D. PIETRAS[1], T. SADOWSKI[1*], M. BONIECKI[2], E. POSTEK[3]

EXPERIMENTAL TESTING OF Al-Si12/SiC INTERPENETRATING COMPOSITES (IPC) IN UNIAXIAL TENSION AND COMPRESSION

The mechanical response of interpenetrating co-continuous composite Al-Si12/SiC$_{3D}$ was described for uniaxial tension and compression. The internal structure of the IPC was examined by optical microscopy and micro-CT. The apparent density and Young's modulus were assessed theoretically and experimentally. Uniaxial tensile tests were performed using the prismatic samples of dimensions 1 mm × 2 mm × 30 mm. Cylindrical samples of diameters $\phi = 5$ mm and height $h = 10$ mm were subjected to quasi-static uniaxial compressive loading. During tests, the side surfaces of the specimen were observed using a digital image correlation system (DIC) to find strain fields and to monitor the surface cracks development in the complex internal microstructure of the IPC.

The analyzed two-phase ICP was manufactured using ceramic foam SiC infiltrated by alloy Al-Si12. This material finds application in cosmic, airplane, or automobile industries, due to their excellent tribological, heat distribution, and ballistic properties.

Obtained results show different modes of microcracking and fracture of cylindrical and prismatic samples. They indicate the substantial influence of the ceramic skeleton on the behavior of the IPC under uniaxial states of loading. Different modes of damage related to the tension or compression loading were described in detail. The results can find application in the designing process of modern co-continuous IPCs and further development of the numerical models of degradation processes.

Keywords: Co-continuous composite; Al-Si12/SiC; interpenetrating composite; tension; and compression tests

1. Introduction

Advanced multiphase composite materials with complex internal architecture are created by different innovative technologies. The composition of these materials results from specific engineering requirements. Different artificial structures with various geometries can be fabricated. One can distinguish the following types of internal structures:

- regular or disordered phases distribution, i.e. matrix and reinforcement in the form of nanoparticles, particles, fibers, whiskers, etc.,
- regular or irregular layered composite structures,
- functional gradation of physical and mechanical properties.

Ceramic composites (CC) and classical polycrystalline ceramics are described in, e.g. [1-8], whereas examples of their modelling with application of (1) mesomechanical method are included in [9-13] or (2) numerical method [14-19]. More complicated internal structures have nanoceramic materials, e.g. [20-22], or functionally graded materials (FGM), e.g. [23-28]. The mixture of plastic matrix and ceramic hard grains leads to the creation of cermets, e.g tungsten carbide/cobalt (WC/Co) or titanium/molybdenum carbides, e.g. [29-38], etc.

A quite different philosophy was implemented in the manufacturing of interphase phase composites (IPCs), Figs 1-4. This complex composite architecture consists of a plastic matrix with content at the level of 80-95%, whereas the reinforcements are in the form of a continuous foam skeleton filled with the matrix alloy, [39-40]. The IPCs belong to the subclass of metal-matrix composites (MMC).

In this paper, we focused on the co-continuous ceramic composite (C4) manufactured of the SiC foam interpenetrated by an aluminium alloy. Among the methods of fabrication of IPCs by filling of ceramic foams by metallic phase, one can distinguish between pressure [41] and pressureless [42] and vacuum feeding technique. It should be mentioned that due to the complex shape of the 3D ceramic skeleton of IPCs the pressured infiltration may lead to the destruction of the brittle ceramic reinforcement structure [41]. The process of manufacturing by using open-cell SiC foam called SiC$_{3D}$ provides the presence of two co-continuous internal networks of constituents in the IPC.

[1] LUBLIN UNIVERSITY OF TECHNOLOGY, 20-618 LUBLIN, 38D NADBYSTRZYCKA STR.., POLAND
[2] ŁUKASIEWICZ RESEARCH NETWORK, INSTITUTE OF MICROELECTRONICS AND PHOTONICS, 02-668 WARSAW, POLAND
[3] INSTITUTE OF FUNDAMENTAL TECHNOLOGICAL RESEARCH, POLISH ACADEMY OF SCIENCES, 02-106 WARSAW, POLAND

* Corresponding author: t.sadowski@pollub.pl

146
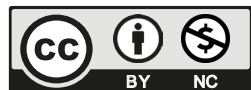
This kind of composite shows excellent physical properties in comparison to others, like low density, large toughness, and little fragility. High thermal conductivity makes, that its various kinds are subject of intense research nowadays. In the literature, we can meet the classic Al/SiC composites in which the aluminium alloy is reinforced by SiC particles (not continuous ceramic phase), Goo et al. [43] and Pan et al. [44]. The tests made by Goo show that the additive of SiC particles to aluminium alloy changes the tensile/compressive toughness ratio and decreases the tensile strength, but improves the tribological properties. The tests performed by Pan show that the composite is applicable to use in temperatures lower than 200°C. Moreover, below 200°C on the surface of the composite, the third body film appears. This phenomenon stabilizes friction properties and reduces wear loss.

The co-continuous Al/SiC_{3D} were investigated by Nong et al. [46] with suggestions for application as ventilated brake disks in high-speed trains. The proposed IPC provides a good transfer of heat generated in the braking process which ensures the uniform distribution of the temperature field in the whole disc. Similar composites were studied by Jiang et al. [47] in application to brake disc in a tribo-couple used for high-speed trains. The main advantage of the manufactured IPC is that up to the initial braking speed of the train lower than 300 km/h abrasive mechanism of damage dominates in this composite and at 350 km/h one can observe oxidation wear and delamination processes. Another form of co-continuous IPCs is 2024Al/ SiC composite with lamellar microstructure described by Liu [48]. This IPC has very high flexural toughness and tensile strength. A similar C4 structure was fabricated via squeezing molten 2024Al into porous SiC preforms produced by freeze casting (Sylajakumari [49]). This new composite has a lamellar microstructure composed of alternating ceramic and metallic lamellar and has the highest strength and toughness. The authors proposed a new method of tribological testing of analysed IPC.

The beneficial ballistic properties of IPCs were reported by Chang et al. [50]. They discovered that the C4 plays an important role to reduce the mechanical impedance mismatch between ceramic plates and metallic ones in various ballistic protection systems. The effect of pores size in SiC foam on the final IPC mechanical properties was examined by Vijayan et al. [40]. The authors focused on the static properties of composites. They found that the compressed specimens have two modes of damage: shear and vertical splitting. The effect of freezing temperature and melt infiltration technique on the microstructure, elastic properties, and compressive stress-strain behaviour of lamellar $Al-Si12/Al_2O_3$ composites was studied in [51].

Most researchers pay attention to the crucial role in mechanical properties of such composite play in the interphases between metal and ceramic, e.g. [48] and Shorowordi et al. [52]. They reported that the two-phases Al-SiC system is reactive and this reaction product – Al_4C_3 – affects the interphase layer degradation. This phenomenon should be minimalised during composite manufacturing by using high silicon content aluminium alloy, e.g. Al-Si12. The observations performed in [48] indicate that the interphase in 2024Al/SiC is brittle and

contains technological cracks after specimen manufacturing. The results presented by Jiang [53] indicate that Mg addition to the aluminium alloy increases the wettability of the interface surface between phases. Moreover, the increase of the holding time during the pressureless infiltration process up to 7 hours reduces the porosity of the IPC and has a beneficial effect on the mechanical properties of C4.

The interesting concept to create a layered version of the FGM based on IPC is presented by Maj et al. [39]. Moreover, this study provides the basic mechanical properties of the IPCs composed of Al-Si12 alloy and Al_2O_3 foam and the influence of the interpenetrating microstructure on the macroscopic bending strength, fracture toughness, hardness, and heat conduction.

It is visible that the methods of manufacturing of IPCs are still developing and their modification to get lack processing-induced flaws and perfect interphase bonding are still required, [54]. Moreover, these materials with 2 co-continuous phases are demanded by modern application in industry, and an assessment of their different mechanical, physical and thermal properties is required. There is also still a lack in the literature of effective numerical models for the calculation of the equivalent mechanical properties of IPCs. These data are important in the future development of these subclass of materials for the design of the technological process of their manufacturing and numerical modelling.

This work aims to present experimental results concerning the estimation of (1) mechanical response and (2) mechanical properties of $Al-Si12/SiC_{3D}$ composite subjected to quasi-static tension and compression. This type of composite is less characterised in the literature in comparison to $Al-Si12/Al_2O_3$, [54]. The measured data are necessary to formulate the effective numerical model at the mesoscale which will be used for designing the process of the IPCs in industry and for assessment of structural element's behaviour subjected to complex loading processes, including high-strain rate deformation or impact, and penetration.

2. Materials and Methods

2.1. Materials – manufacturing of $Al-Si12/SiC_{3D}$ IPC

The analysed $Al-Si12/SiC_{3D}$ IPC was fabricated by squeeze casting technology after infiltration under pressure the 20-PPI SiC preform (Fig. 1) by the molten Al-Si12 aluminium alloy, [39]. To avoid premature melt solidification and infiltration under the pressure of 100 MPa, the SiC preform was preheated up to 700°C. The used pressure ensured an exact infiltration of the SiC skeleton penetrating very small pores. The external pressure must overcome the capillarity resistance of the preform. After that, a stable infiltration phase follows where the function pressure value to time is linear until the melt filled up the SiC preform. At this point, a pressure jumps to the maximum value equal to 100 MPa, and compression of residual air takes place. The finally fabricated IPC has the following nominal volume fractions equal to 85% of aluminium alloy and 15% of SiC skeleton.

The structure of brittle SiC preform was observed by optical microscope Keyence, Fig. 1. One can notice, that all the observed cells are open, but some ceramic struts are micro-cracked during the foam manufacturing. It means that the initial skeleton structure is not perfect.
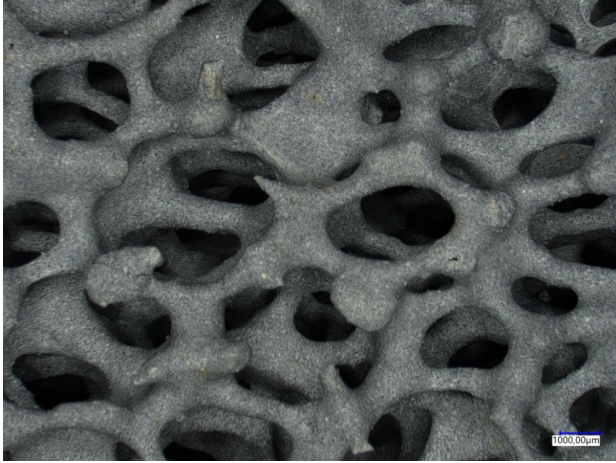

Fig. 1. The optical microscopic photograph of the SiC skeleton (20 PPI)

The final IPC was observed by microscope and micro-CT, Fig. 2, where an exemplary cross-section of considered material is presented. It is visible that the composite consists of three main phases: SiC foam elements, Al-Si12 matrix, and macro porosity. At the foam boundaries, many flaws and huge thickness reaction products between aluminium alloy and SiC foam are imperceptible. Therefore, it means that the process of infiltration was performed successfully. The internal structure of silicon carbonate foam and aluminium matrix probably contains mesoporosity.
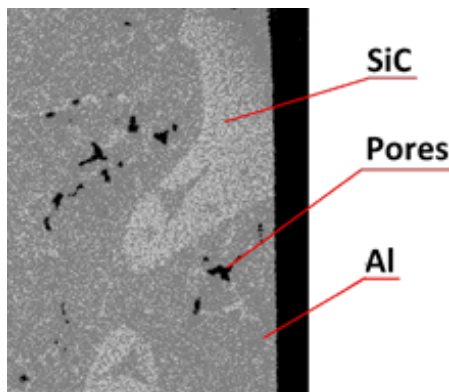

Fig. 2. The micro-CT photography of an exemplary cross-section of the specimen

2.2. Physical and mechanical properties

2.2.1. Density and porosity of the IPC

The apparent density of the Al-Si12/SiC$_{3D}$ IPC was assessed by using the Archimedes method in which the mass of specimens

in air m_a and the mass of specimens in water are measured. Subsequently, the density is computed by the following expression:

$$\rho_{sp} = \frac{m_a}{m_a - m_w} \rho_w \qquad (1)$$

where ρ_w is water density. In this case, ρ_w was assumed equal to 1000 kg/m^3. The density was determined for cylindrical specimens with a diameter of 5 mm, a height of 10 (slender), and cylindrical with a diameter of 8 mm and height of 4 mm called "stocky" specimens presented in Fig. 3. and Fig. 4.

Fig. 3. The view of slender specimens (side)

Fig. 4. The view of stocky specimens (top surface)

The standard deviation was computed as follows:

$$SD = \sqrt{\frac{\sum_{i=1}^{n}\left(x_i - x_{AVG}\right)^2}{n-1}} \qquad (2)$$

is the mean value of the parameter for all tested specimens, and n is the number of tested specimens. The relative standard deviation was assessed according to the following formula:

$$RSD = \frac{SD}{AVG} \cdot 100\% \qquad (3)$$

The constituents of the considered IPC: SiC has a nominal density of 3215 kg/m^3, whereas Al-Si12 has a density equal to 2700 kg/m^3. The theoretical IPCs density according to Reuss or Voigt rules of the mixture ([55]) should be within these limits

148

according to the following expression for the upper limit (Reuss rule of mixture)

$$\rho^{(Re)} = \rho_{\text{Al-Si12}} \cdot 0.85 + \rho_{\text{SiC}} \cdot 0.15 = 2\ 777\ \frac{\text{kg}}{\text{m}^3} \qquad (4)$$

and the lover limit (Voight rule of mixture):

$$\rho^{(Vo)} = \left(\frac{0.85}{\rho_{\text{Al-Si12}}} + \frac{0.15}{\rho_{\text{SiC}}} \right)^{-1} = 2\ 766\ \frac{\text{kg}}{\text{m}^3} \qquad (5)$$

The results of composite density measurements by using the Archimedes method for stocky specimens are presented graphically in Fig. 5 and for slender specimens in Fig. 6.
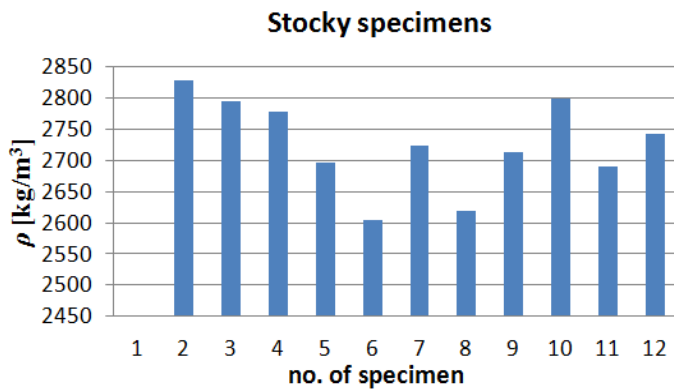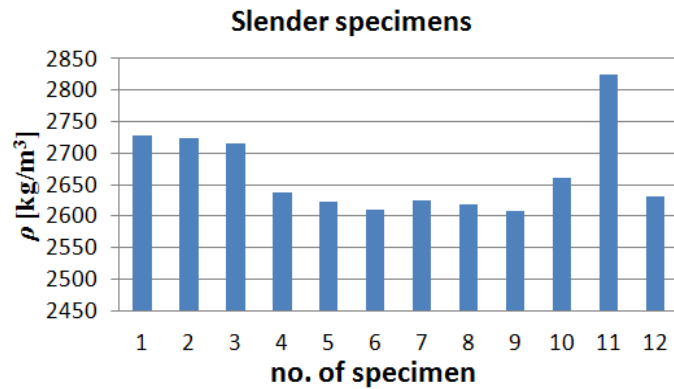

Fig. 5. Bulk density for "stocky" specimens

Fig. 6. Bulk density for slender specimens

The achieved results for particular specimens are collected in TABLE 1. It is visible that average values both for stocky and slender specimens are under the lower limit of density according to the rule of mixture. However, the range assessed by the rules of the mixture is consistent with the derived results after taking into account the standard deviation. The relative

standard deviation for analyzed specimens is smaller than 3%, which proves the high repeatability of the material and specimen manufacturing process.

The porosity of the analysed IPC specimens is equal to 2-3%.

2.2.2. The theoretical value of Young's modulus assessed by the rule of mixtures

The upper value of the expected theoretical Young's modulus of elasticity according to the linear rule of mixture (Voigt) [55] is equal to:

$$E_{\text{Al-Si12/SiC}}^{(Vo)} = E_{\text{Al-Si12}} \cdot 0.85 + E_{\text{SiC}} \cdot 0.15 = 129.3\ \text{GPa} \qquad (6)$$

The $E_{\text{Al-Si12}}$ is equal to 76.2 GPa [56] and E_{SiC} equal to 410 GPa.

The lover limit is equal to (Reuss rule of mixture):

$$E_{\text{Al-Si12/SiC}}^{(Re)} = \left(\frac{0.85}{E_{\text{Al-Si12}}} + \frac{0.15}{E_{\text{SiC}}} \right)^{-1} = 86.63\ \text{GPa} \qquad (7)$$

The above values were compared to the experimental data presented below.

2.3. Experimental Methods for IPCs

2.3.1. Uniaxial tension tests

Uniaxial tensile tests were done using prismatic samples with the following dimensions 1 mm × 2 mm × 30 mm, Fig. 7. The tests were performed using Zwick/Roell machine (10 kN) under constant displacement rate of piston equal to 1 mm/min.

Fig. 7. Specimens used in a uniaxial tension test

TABLE 1

Densities ρ of the investigated IPCs

Specimen No	1	2	3	4	5	6	7	8	9	10	12	AVG	SD	RSD
Stocky [kg/m³]		2827.7	2795.5	2778.6	2695.9	2604.9	2722.8	2619.3	2712.8	2799.1	2691.1	2724.8	71.9	2.64
Slender [kg/m³]	2727.3	2724.7	2715.3	2637.2	2622.3	2610.6	2625.0	2618.2	2608.8	2660.7	2825.5	2670.5	66.0	2.47

During samples deformation, the complex internal structure of the IPC degrades by initiation and growth of various micro-cracking processes in:

- brittle ceramic foam,
- interfaces between ceramic and metallic phases,
- metallic matrix.

The response of the material to the applied deformation process is related to the dominant failure mode in the particular specimen, which is induced by its specific internal microstructure. Therefore, the tested specimens were divided into two groups having different shapes of stress-elongation curves.

The first group of specimens with typical non-linear behaviour is presented in Fig. 8. The whole stress-elongation curves consist of 3 characteristic parts. In the early stage of the deformation process, the correlation is approximately linear and inclination angles are similar for most of the specimens. Upon reaching the critical failure point, specimens 2 and 24, carrying force, suddenly drop to zero. In the case of specimen 6, we observed a slow decrease of the carrying force just after peeking of stress. The other specimens behave like quasi-brittle materials. In this group of specimens, the ceramic phase has a dominant role in carrying the load. The quasi-brittle behaviour is caused by the locking of fractured ceramic foam beams in the metallic phase, which is a local effect. This phenomenon increases absorbed energy by IPC during gradual failure.
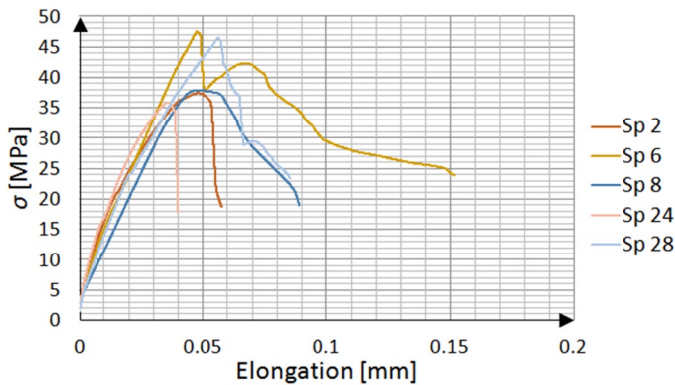
The stress-elongation curves for the second group of specimens are presented in Fig. 9. In these cases, the deformation processes are more complex in comparison to the first group. The beginning of the loading process up to 15 MPa is quasi-linear. After this stage, the material behaves like ideally plastic until the second strengthening occurs. This plateau has a different length, which depends on the internal structure of the IPC. Then the curves become strongly non-linear and after maximum, the final failure begins. The sample's mechanical responses are similar to that of the first group, i.e. specimen 17 ruptures suddenly. Sample 25 shows the locking effect of the ceramic struts and the second plateau line takes place before the sudden final failure. Sample 16 has quasi-brittle behavior with a smooth linear decrease after the peaking of stress. The gradual degradation process of the sample can be modelled by a bi-linear damage law.
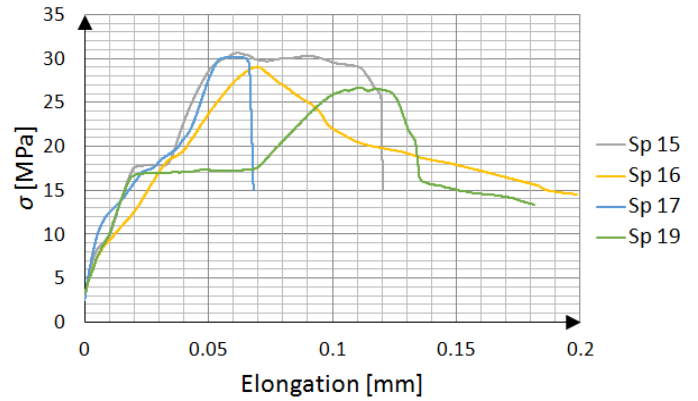
Fig. 9. The stress-elongations curves in uniaxial tension for the second group of specimens

The major characteristics of all stress-elongation curves are collected in TABLE 2.

The experimentally determined averaged value of the modulus of elasticity, assessed for the linear part of the plot stress-strain relations, is equal to $E^{(t)}_{\text{Al-Si12/SiC}} = 9.27 \pm 0.7$ GPa and is less than Voigt and Reuss's estimation by the rule of mixtures, Eqs (6) and (7).

Fig. 8. The stress-elongations curves in uniaxial tension for the first group of specimens

TABLE 2

The major characteristics of the stress-elongation curves for all tested specimens

Group 1 (G1)				Group 2 (G2)		
SP no	$E^{(t)}_{\text{Al-Si12/SiC}}$	$\sigma^{(t)}_{\text{Al-Si12/SiC}}$	$\varepsilon^{(t)}_{\text{Al-Si12/SiC}}$	SP no	$\sigma^{(t)}_{\text{Al-Si12/SiC}}$	$\varepsilon^{(t)}_{\text{Al-Si12/SiC}}$
	GPa	MPa	%		MPa	%
2	8.676	37.446	0.479	15	30.662	0.620
6	9.175	47.575	0.476	16	29.059	0.697
8	8.552	37.889	0.500	17	30.195	0.620
24	10.396	35.876	0.351	19	26.642	1.114
28	9.573	46.487	0.561	—	—	—
AVG	9.274	41.055	0.473	AVG	29.140	0.763
SD	0.669	4.937	0.068	SD	1.555	0.205
RSD	7.212	12.026	14.451	RSD	5.337	26.905

2.3.2. Uniaxial compression tests

The uniaxial compression tests of the SiC foam, matrix material Al-Si12 and composite were performed by using MTS 810 Bionix machine and "slender" cylindrical specimens. The ratio of height to diameter is 2, i.e. the uniaxial compression in the middle part of the samples was assured. The tests were performed with a constant displacement rate of the machine piston equal to 0.2 mm/min.

The stress in all cases is defined as the ratio of acting force F to the initial area of the initial cross-section area of the specimen A_{sp}:

$$\sigma = \frac{F}{A_{sp}} \qquad (8)$$

The side surface of compressed specimens was observed by the digital image correlation (DIC) system ARAMIS during the whole deformation process. The components of the Lagrange strain tensor. The components of the Lagrange strain tensor ε_{ki} were computed by the ARAMIS system according to:

$$\varepsilon_{ik} = \frac{1}{2}\left(\frac{\partial u_i}{\partial x_k} + \frac{\partial u_k}{\partial x_i} + \frac{\partial u_m}{\partial x_i}\frac{\partial u_m}{\partial x_i} \right) \qquad (9)$$

where u_i are components of the displacement vector $\vec{u}$, and $\{x_k\}$ is the coordinate system. The ARAMIS system estimated the state of strains, i.e. both the vertical strains ε_{yy} and horizontal ε_{xx} strains. The ε_{yy} is responsible for the creation of horizontal cracks and ε_{xx} causes the initiation and growth of vertical cracks during deformation.

2.3.2.1. Compressive strength and elastic modulus of the SiC foam

The exemplary stress-strain curve for the SiC foam performed with MTS 810 and a force transducer 2.5 kN, is plotted in Fig. 10. The experimental samples are cubic with a dimension of 10 mm. The maximum compressive strength of the foam was equal to $\sigma_{SiC}^{(c)} = 1.15 \pm 0.12$ MPa, whereas Young's modulus was assessed for the linear part of the plot equal to $E_{SiC}^{(c)} = 39 \pm 5$ MPa.
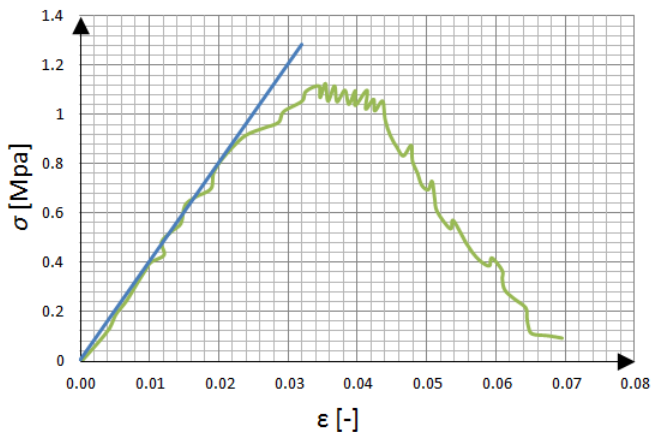

Fig. 10. Exemplary stress-strain curve for the used SiC foam

2.3.2.2. Compressive strength and elastic modulus of the Al-Si12 matrix

Fig. 11 presents the exemplary compression curve for the pure Al-Si12 metallic matrix, performed with "stocky" shaped cylindrical specimens ($\phi = 5$ mm; $h = 10$ mm). The modulus of elasticity under compression is equal to $E_{\text{Al-Si12}}^{(c)} = 67.60 \pm 9.32$ MPa, whereas the compressive strength $\sigma_{\text{Al-Si12}}^{(c)} = 262 \pm 20$ MPa for $\varepsilon = 0.5$.
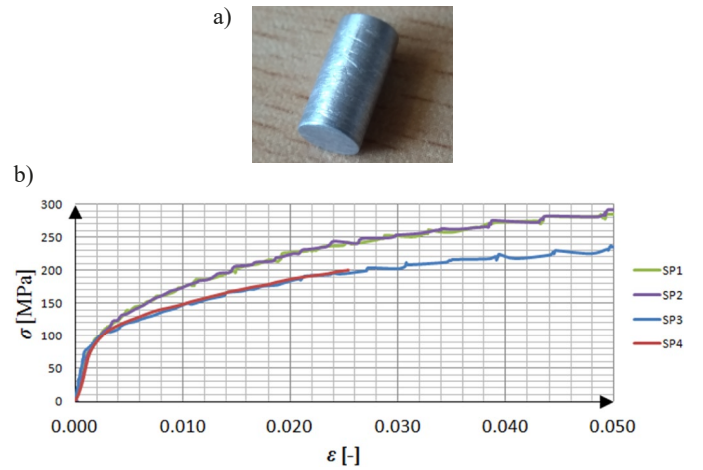

Fig. 11. Exemplary curve for Al-Si12 matrix material: a) testing sample, b) stress-strain curve

2.3.2.3. Compressive strength and elastic modulus of the Al-Si12/SiC₃D matrix

The observations of the mechanical response of considered Al-Si12/SiC$_{3D}$ IPC under the compressive deformation process were monitored by the DIC system starting from the initial elastic stages, through gradual degradation, up to the final failure ($t = 240$ s). Fig. 12 presents the correlation of loading force F with time t. The compressive state of loadings is marked by negative values of F. Up to $t = 80$ s (red vertical line, Fig. 12), the deformation process of the sample is elastic. Is visible a highly non-uniform distribution of both Lagrange strain tensor components ε_{xx} and ε_{yy}. The component ε_{yy} indicates the regions with small values of strains that are located in regions corresponding to ceramic fraction distribution. One can notice, that the area of regions with smaller strains is usually higher than the area of the ceramic phase. The highest values of ε_{yy} strains, marked by blue colour, are located at the ceramic-metal interfaces. It means, that even in the linear pure elastic macroscopic response of the Al-Si12/SiC$_{3D}$ IPC under compressive loading the continuity of the composite between metal and ceramic phases is destroyed. It indicates that the critical cohesive forces between both phases are small, due to the technological process during material cooling. The middle values of vertical strains in direction Y, marked by green colour, are present mainly in places of occurrence of higher concentration of metallic phase. ε_{xx} has more uniform distribution in comparison to ε_{yy}. The largest area

of the observed side surface of the specimen has low values ε_{xx} marked by blue colour. The middle values of ε_{xx} (green colour) are visible mainly in the bottom part of the specimen which dominates the aluminium phase. The largest values ε_{xx} strains occur in the debonded interfaces, which indicate cracked parts of the composite structure.
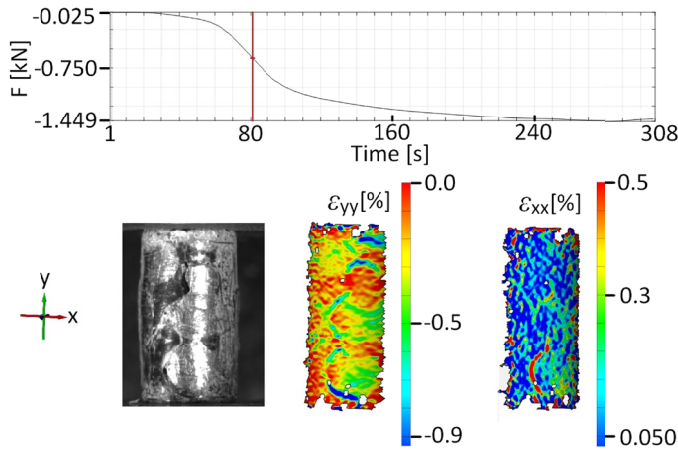

Fig. 12. The response of slender specimen to applied uniaxial compressive loadings – linear elastic range (t = 80 s)
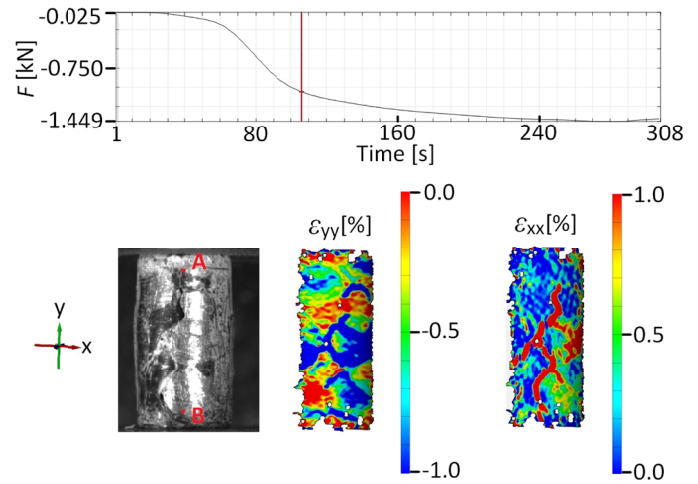

Fig. 13. The response of slender specimen to applied uniaxial compressive loadings – microcracking stage (t = 106 s)

is more than 2 times lower than assessed by the Reuss rule of mixture, Eq. (7).

2.3.2.4. Comparisons of obtained results

It is necessary to point out that the elastic properties of considered composite for compression loadings are other than for tension. All experimentally estimated Young's modules are collected in Fig. 15.

In the case of modulus of elasticity the material is more than 5.2 times higher for compression in comparison to tension, ($E^{(c)}_{\text{Al-Si12/SiC}}/E^{(t)}_{\text{Al-Si12/SiC}} = 5.2$). This effect results from very weak interfaces of both phases, where some amount of porosity – is about 3%. These discontinuities have a higher influence during tension tests – the rapid growth of cracks during loading.

The analysed IPC has 3.9 times higher compressive strength in comparison to tension one ($\sigma^{(c)}_{\text{Al-Si12SiC}}/\sigma^{(t)}_{\text{Al-Si12SiC}}$) which is characteristic of brittle materials, Fig. 16.

The plastic behaviour starts from stress higher than 65 MPa for Al-Si12 and IPC which is approximately 1.58 times more for specimens from 1 group of response (G1) in tension and
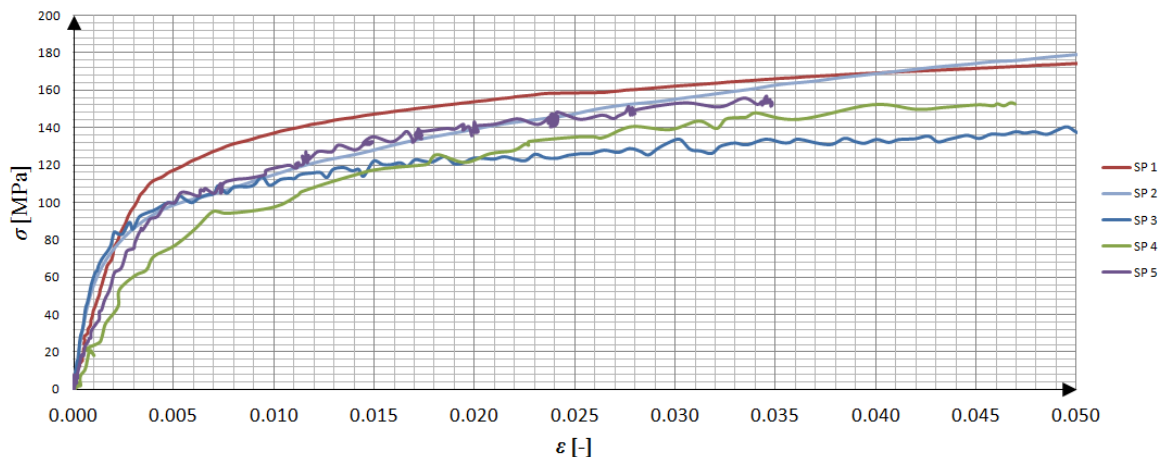
The response of tested material in the post-linear-elastic behaviour state of deformation exhibiting distributed intensive microcracking process is presented in Fig. 13, (t = 106 s). There is a visible progress of strain increase in comparison to Fig. 12. In the Al-Si12 phase at the centre part of the specimen, one can observe the concentration of vertical strains ε_{yy}.

The stress-strain relation describing the macroscopic response of the sample was measured between points A and B (Fig. 13) and presented in Fig. 14. The shape of this relation for the IPC corresponds to the behaviour of a plastic material with non-linear hardening because the volume content of the Al-Si12 is approximately 85%.

The initial stage of the stress-strain relation is linear-elastic up to 80 MPa. The modulus of elasticity for tested IPC under compression is assessed for the linear parts of the stress-strain relations. It is equal to $E^{(c)}_{\text{Al-Si12/SiC}} = 48.238 \pm 18.6$ GPa and

Fig. 14. The stress-strain relation for the IPC composite specimen in uniaxial compression
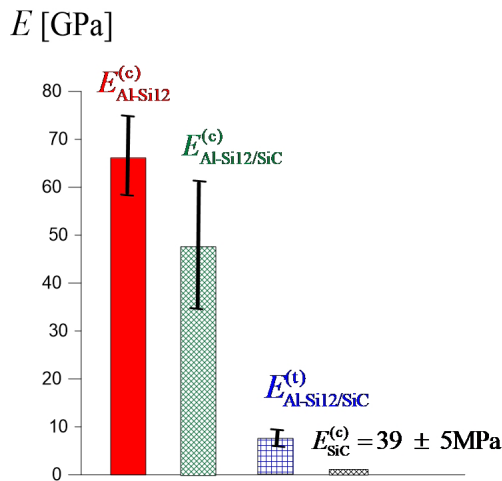
152

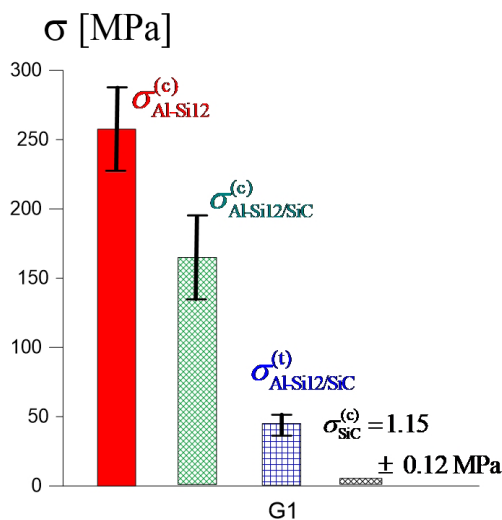Fig. 15. Comparison of Young's modulus for tension and compression

Fig. 16. Comparison of the uniaxial tension and compression strengths for strains equal to $\varepsilon = 0.05$

2.24 times more than values recorded for specimens from the second group (G2) of tension. The compressive strength of the matrix material Al-Si12 was investigated in [57], where the maximum compressive strength at the ambient temperature was 285 MPa, i.e. slightly more than in the present investigations.

3. Conclusions

This study performed the uniaxial tension of prismatic specimens and uniaxial compression of cylindrical specimens of modern co-continuous composite Al-Si12/SiC$_{3D}$ made of silicon carbide foam and aluminium alloy. The experiments done with the IPC led to the formulation of the following conclusions:

- theoretically calculated Young's modules according to the rule of mixtures is fare from the experimental estimations,
- the performed tests show that the interfaces between the metal and ceramic phases are substantially weak. The low values of Young's modulus for tension confirm that during the manufacturing process micro-, and mesopores (see Fig. 2), and other discontinuities at interfaces are introduced to the internal structure of the IPCs,

- different values of Young's modules for the composite in tension and compression were experimentally observed. The ratio $E^{(c)}_{\text{Al-Si12/SiC}} / E^{(t)}_{\text{Al-Si12/SiC}} = 5.2$, i.e. the modulus of elasticity in compression is 3 times higher concerning tension,

- introduction to the AlSi12 the ceramic skeleton SiC leads to the significant decrease of the elastic modulus of the composite in comparison to the pure matrix, i.e. the ratio $E^{(t)}_{\text{Al-Si12/SiC}} / E^{(c)}_{\text{Al-Si12}}$ is equal to 0.14, and $E^{(c)}_{\text{Al-Si12/SiC}} / E^{(c)}_{\text{Al-Si12}} = 0.71$. This results from different damage processes which develop in tension and compression. The weak interfaces and porosity particularly speed up the gradual degradation process under tension, where cracks extend in a direction perpendicular to the loading axis. In compression states, where micro-cracks extend mainly along the vertical direction causing bulge and fragmentation of samples, the damage process is highly resistant and the failure of samples requires much more energy and level of loading,

- the behavior of composite exhibits brittle properties which are expressed by the high ratio between compressive critical load and tension $\sigma^{(c)}_{\text{Al-Si12SiC}} / \sigma^{(t)}_{\text{Al-Si12SiC}} = 3.9$.

The obtained results will lead to the formulation of the advanced numerical model of the composite, using different approaches for modelling complex phenomena occurring at interfaces between two phases, e.g. [58,59].

The next step in experimentation will be an assessment of the dynamic mechanical properties of the IPC using a Split Hopkinson Pressure Bar and penetration stand. Estimating the dynamical response of the analysed composite results forms its applications to various ballistic systems.

REFERENCES

[1] T. Fett, D. Munz, Mechanical Properties, Failure Behaviour, Materials Selection, Ceramics, Springer, Berlin, Heidelberg, New York (1999). DOI: https://dx.doi.org/10.1007/978-3-642-58407-7

[2] R.W. Rice, Mechanical Properties of Ceramics and Composites – Grain and Particle Effects, New York, Basel, Marcel Dekker, Inc. (2000). ISBN: 0-8247-8874-5

[3] W. Krenkel (ed.), Ceramic matrix composites. Fiber-reinforced ceramics and their applications, Wiley-VHC (2010).

[4] L. Li High temperatures mechanical behavior of ceramic matrix composites, Wiley-VHC GmbH (2010). ISBN: 3527349030.

[5] J.P. Davim (ed.), Ceramic matrix composites, de Guyter GmbH (2016). ISBN: 3110352842.

[6] L.A. Gömze, L.N. Gömze, Alumina-based hetero-modulus ceramic composites with extreme dynamic strength – phase transformation of Si_3N_4 during the high-speed collision with metallic bodies, Ėpitöanyag: JSBCM. **61**, 38-42 (2009).
DOI: https://dx.doi.org/10.14382/epitoanyag-jsbcm.2009.7

[7] M. Szutkowska, M. Podsiadło, T. Sadowski, P. Figiel, M. Boniecki, T. Polczyk, A novel approach by spark plasma sintering to the improvement of mechanical properties of titanium carbonitride-reinforced alumina ceramic, Molecules **26** 1344 (2021).
DOI: https://doi.org/10.3390/molecules26051344

[8] M. Boniecki, T. Sadowski, P. Gołębiewski, H. Węglarz, A. Piątkowska, M. Romaniec, K. Krzyżak, K. Łosiewicz, Mechanical properties of alumina/zirconia composites, Cer. Int. **46**, 1033-1039 (2020).
DOI: https://doi.org/10.1016/j.ceramint.2019.09.068

[9] T. Sadowski, S. Samborski, Modelling of porous ceramics response to compressive loading, J. Am. Cer. Soc. **86**, 2218-2221 (2003).
DOI: https://dx.doi.org/10.1111/j.1151-2916.2003.tb03637.x

[10] T. Sadowski, S. Samborski, Prediction of mechanical behaviour of porous ceramics using mesomechanical modelling, Comp. Mat. Sci. **28**, 512-517 (2003).
DOI: https://doi.org/10.1016/j.commatsci.2003.08.008

[11] Sadowski, T., Modelling of semi-brittle ceramics behavior under compression, Mech. Materials, **18**, 1-16 (1994).
DOI: 10.1016/0167-6636(94)90002-7

[12] T. Sadowski, Gradual degradation in two-phase ceramic composites under compression, Comput. Mat. Sci. 64 (2012) 209-211.
DOI: https://doi.org/10.1016/j.commatsci.2012.01.034

[13] T. Sadowski, S. Samborski, Development of damage state in porous ceramics under compression, Comp. Mater. Sci. **43**, 75-81 (2008).
DOI: https://doi.org/10.1016/j.commatsci.2007.07.041

[14] H.D. Espinoza, P.D. Zavattieri, A grain level model for the study of failure initiation and evolution in polycrystalline brittle materials. Part I: Theory and numerical implementation, Mech. Mater. **35**, 333-364 (2003).
DOI: https://doi.org/10.1016/S0167-6636(02)00285-5

[15] H.D. Espinoza, P.D. Zavattieri, A grain level model for the study of failure initiation and evolution in polycrystalline brittle materials. Part II: Numerical examples, Mech. Mater. **35**, 365-394 (2003).
DOI: https://doi.org/10.1016/S0167-6636(02)00287-9

[16] D. Ghosh, M. Banda, S. Akurati, H. Kang, O. Fakharizadeh, On the brittle fracture characteristics of lamella walls of ice-templated sintered alumina scaffolds and effects of platelets, Scripta Mater. **138**, 139-144 (2017).
DOI: https://doi.org/10.1016/j.scriptamat.2017.05.049

[17] T. Sadowski, B. Pankowski, Numerical modelling of two-phase ceramic composite response under uniaxial loading, Comp. Struct. **143**, 388-394 (2016).
DOI: https://doi.org/10.1016/j.compstruct.2016.02.022

[18] T. Sadowski, G. Golewski, Effect of aggregate kind and graining on modelling of plain concrete under compression, Comp. Mat. Sci. **43**, 119-126 (2008).
DOI: https://doi.org/10.1016/j.commatsci.2007.07.037

[19] E. Postek, T. Sadowski, Impact model of the Al_2O_3/ZrO_2 composite by peridynamics, Compos. Struct. **271**, 114071 (2021).
DOI: https://doi.org/10.1016/j.compstruct.2021.114071

[20] A. Makholouf, D. Scharnweber, Handbook of nanoceramics and nanocomposite coatings and materials, Elsevier (2015).

[21] M. Winterer, Nanocrystalline ceramics, synthesis and structure, Springer, Berlin, (2002).
DOI: https://doi.org/10.1007/978-3-662-04976-1

[22] C.C. Koch, I.A. Ovid'ko, S. Seal, S. Veprek, Structural nanocrystalline materials: fundamentals and applications, Cambridge, Cambridge Univ. Press, 2007.
DOI: https://doi.org/10.1002/anie.200685538

[23] B. Saleh, J. Jiang, R. Fathi, T. Al-Habibi, Q. Xu, L. Wang, D. Song, A. Ma, 30 years of functionally graded materials: An overview of manufacturing methods, applications and future challenges, Compos. Part B **201**, 108376 (2020).
DOI: https://doi.org/10.1016/j.compositesb.2020.108376

[24] E. Pazera, J. Jędrysiak, Thermoelastic phenomena in transversally graded laminates, Comp. Struct. **134**, 663-671 (2015).
DOI: https://doi.org/10.1016/j.compstruct.2015.08.081

[25] T. Sadowski, P. Golewski, The influence of quantity and distribution of cooling channels of turbine elements on level of stresses in the protective layer TBC and the efficiency of cooling, Comput. Mat. Sci. **52**, 293-297 (2012).
DOI: https://doi.org/10.1016/j.commatsci.2011.02.027

[26] T. Sadowski, P. Golewski, Multidisciplinary analysis of the operational temperature increase of turbine blades in combustion engines by application of the ceramic thermal barrier coatings (TBC), Comput. Mat. Sci. **50**, 1326-1335 (2011).
DOI: https://doi:10.1016/j.commatsci.2010.05.032

[27] V. Ivanov, T. Sadowski, D. Pietras, Crack propagation in the functionally graded strip under thermal shock, Eur. Phys. J. Special Topics **222**, 1587-1595 (2013).
DOI: https://doi.org/10.1140/epjst/e2013-01947-3

[28] T. Sadowski, A. Neubrand, Estimation of the crack length after thermal shock in FGM Strip, Int. J. Fract. **127**, L135-L140 (2004).

[29] K.S. Ravichandran, Fracture toughness of two-phase WC-Co cermets, Acta Metal. Mater. **42**, 143-150 (1994).
DOI: https://doi.org/10.1016/0956-7151(94)90057-4

[30] S. Hönle, S. Schmauder, Micromechanical simulation of cracks growth in WC/Co using embedded unit cells, Comput. Mater. Sci. **13**, 56-60 (1998).
DOI: https://doi.org/10.1016/S0927-0256(98)00045-7

[31] W. Li, H. Wang, L. Wang, C. Hou, X. Song, X. Liu, X. Han, In situ of fracture behavior of ultrafine WC-Co cemented carbide, Mat. Res. Letters **5**, 55-60 (2017).
DOI:https://doi.org/10.1080/21663831.2016.1208300

[32] T. Sadowski, T. Nowicki, Numerical investigation of local mechanical properties of WC/Co composite, Comput. Mat. Sci. **43**, 235-241 (2008).
DOI: https://doi.org/10.1016/j.commatsci.2007.07.030

[33] D. Tkalich, G. Cailletauld, V.Y. Yestrebov, A. Kane, A micromechanical constitutive modelling of WC hardmetals using finite-element and uniform models. Mech. Mater. **105**, 166-187 (2017).
DOI: https://doi.org/10.1016/j.mechmat.2016.11.007

[34] T. Sadowski, S. Hardy, E. Postek, Prediction of the mechanical response of polycrystalline ceramics containing metallic intergranular layers under uniaxial tension, Comput. Mat. Sci. **34**, 46-63 (2005). DOI: https://doi.org/10.1016/j.commatsci.2004.10.005

[35] T. Sadowski, S. Hardy, E. Postek, A new model for the time-dependent of polycrystalline ceramic materials with metallic inter-granular layers under tension, Mat. Sci. Eng. A. **424** 230-238 (2006). DOI: https://doi.org/10.1016/j.msea.2006.03.004

[36] T. Sadowski, E. Postek, C. Denis, Stress distribution due to discontinuities in polycrystalline ceramics containing metallic inter-granular layers, Comput. Mat. Sci. **39** 230-236 (2007). DOI: https://doi.org/10.1016/j.commatsci.2006.03.022

[37] H. Dębski, T. Sadowski, Modelling of microcracks initiation and evolution along interfaces of the WC/Co composite by the finite element method, Comput. Mat. Sci. **83**, 403-411 (2014). DOI: https://doi.org/10.1016/j.commatsci.2013.11.045

[38] E. Postek, T. Sadowski, Assessing the Influence of Porosity in the Deformation of Metal-Ceramic Composites, Comp. Interf. **18**, 57-76 (2011). DOI: https://doi.org/10.1163/092764410X554049

[39] J. Maj, M. Basista, W. Węglewski, K. Bochenek, A. Strojny-Nędza, K. Naplocha, T. Panzner, M. Tatarková, F. Fiori, Effect of microstructure on mechanical properties and residual stresses in interpenetrating aluminum-alumina composites fabricated by squeeze casting, Mater. Sci. Eng. A **715** 154-162 (2018). DOI: https://doi.org/10.1016/j.msea.2017.12.091

[40] K Vijayan, S. Ramalingam, M.R.A. Sadik, A.S. Prasanth, J. Nampoothiri, J.P. Escobedo-Diaz, K. Shankar, Fabrication of Co-Continuous ceramic composite (C4) through gas pressure infiltration technique, Mater. Today: Proc. **46** 1013-1016 (2021). DOI: https://doi.org/10.1016/j.matpr.2021.01.212

[41] R. Gil, A. Jinnapat, A.R. Kennedy, Pressure-assisted infiltration of molten aluminum into open-cell ceramic foams: experimental observations and infiltration modelling, Compos. Part A **43**, 880-884 (2012).
DOI: https://doi.org/10.1016/j.compositesa.2012.02.001

[42] H. Chang, R.L. Higginson, J.G.P. Binner, Interface study by dual-beam FIB TEM in a pressureless infiltrated Al(Mg)-Al2O3 interpenetrating composite, J. Microsc. **233**, 132-139 (2009). DOI: https://doi.org/10.1111/j.1365-2818.2008.03103.x

[43] H. Chang, R. Higginson, J. Binner, Microstructure and property characterisation of 3-3 Al(Mg)/Al2O3 interpenetrating composites produced by a pressureless infiltration technique, J. Mater. Sci. **45**, 662-668 (2010). DOI: https://doi.org/10.1007/s10853-009-3983-9

[44] B.-C. Goo, M.-H. Kim, Characteristics of A356/SiCp and A390/SiCp composites, J. Mech. Sci. Technol. **26** (7), 2097-2100 (2012). DOI: https://doi.org/10.1007/s12206-012-0522-4

[45] L.K. Pan, J.M. Han, Z.Y. Yang, J.L. Wang, X. Li, Z.Q. Li, W.J. Li, Temperature effects on the friction and wear behaviors of SiCp/A356 composite against semimetallic materials, J. Adv. Mater. Sci. Eng. **2017**, 1-12 (2017).
DOI: https://doi.org/10.1155/2017/1824080

[46] X.D. Nong, Y.L. Jiang, M. Fang, L. Yu, C.Y. Liu, Numerical analysis of novel SiC3D/Al alloy co-continuous composites ventilated brake disc, Int. J. Heat Mass Transf. **108**, 1374-1382 (2017). DOI: https://doi.org/10.1016/j.ijheatmasstransfer.2016.11.108

[47] L. Jiang, Y. Jiang, L. Yu, H. Yang, Z. Li, Y. Ding, G. Fu, Fabrication, microstructure, friction and wear properties of SiC3D/Al brake disc-graphite/SiC pad tribo-couple for a high-speed train, Trans. Nonferrous Met. Soc. China **29**, 1889-1902 (2019).
DOI: https://doi.org/10.1016/S1003-6326(19)65097-1

[48] Q. Liu, F. Ye, Y. Gao, S. Liu, H. Yang, Z. Zhou, Fabrication of a new SiC/2024Al co-continuous composite with lamellar microstructure and high mechanical properties, J. Alloys Compounds **585**, 146-153 (2014).
DOI: https://doi.org/10.1016/j.jallcom.2013.09.140

[49] P.A. Sylajakumari, R. Ramakrishnasamy, G. Palaniappan, Taguchi grey relational analysis for multi-response optimization of wear in co-continuous composite, Materials, **11**, 1743 (2018).
DOI: https://doi.org/10.3390/ma11091743

[50] H. Chang, J. Binner, R. Higginso Preparation and characterisation of ceramic-faced metal-ceramic interpenetrating composites for impact applications, J Mater. Sci. **46**, 5237-5244 (2011).
DOI: https://doi.org/10.1007/s10853-011-5461-4

[51] S. Roy, J. Frohnheiser, A. Wanner, Effect of ceramic preform freeze-casting temperature and melt infiltration technique on the mechanical properties of a lamellar metal/ceramic composite, J. Comp. Mater. **54**, 2001-2011 (2020).
DOI: https://doi.org/10.1177/0021998319890661

[52] K.M. Shorowordi, T. Laoui, A.S.M.A. Haseeb, J.P. Celis, L. Froyen Microstructure and interface characteristics of B4C, SiC and Al2O3 reinforced Al matrix composites: a comparative study, J. Mater. Process. Technol. **142**, 738-743 (2003).
DOI: https://doi.org/10.1016/S0924-0136(03)00815-X

[53] G. Jiang, L. Ding, L. Yiu, W. Xiong, Y. Ni, X. Yao, J. Xu, W. Li, Study on the SiC-Al Co-continuous Phase, J. Mater. Process. Technol. **745-746**, 577-581 (2013).
DOI: https://doi.org/10.4028/www.scientific.net/MSF.745-746.577

[54] M. Basista, J. Jakubowska, W. Węglewski, Processing induced flaws in aluminum-alumina interpenetrating phase composites, Adv. Eng. Mater. **19**, 1700484 (2017).
DOI: https://doi.org/10.1002/adem.20170048

[55] D.K.Y. Tam, S. Ruan, P. Gao, T. Yu, High-performance ballistic protection using polymer nanocomposites, in Advances in Military Textiles and Personal Equipment (Ed. E. Sparks), 213-237 (2012).

[56] F. Lasagni, H.P. Degischer, Enhanced Young's modulus of Al-Si alloys and reinforced matrices by co-continuous structures, J. Compos. Mat. **44**, 739-755 (2010).
DOI: https://doi.org/10.1177/0021998309347649

[57] A. Kurzawa, J.W. Kaczmar, Compressive strength of EN AC-44200 based composite materials strengthened with a-Al$_2$O$_3$ particles, Arch. Foundry Eng. **17**, 43-48, (2017).
DOI: https://doi.org/10.1515/afe-2017-0049

[58] L. Marsavina, T. Sadowski, Fracture parameters at bi-material ceramic interfaces under the bi-axial state of stress, Comput. Mat. Sci. **45**, 693-697 (2009).
DOI: https://doi.org/10.1016/j.commatsci.2008.06.005

[59] L. Marsavina, T. Sadowski, Kinked cracks at a bi-material ceramic interface – numerical determination of fracture parameters, Comput. Mat. Sci. **44**, 941-950 (2009).
DOI: https://doi.org/10.1016/j.commatsci.2008.07.005